Numerical Modeling for Shoulder Injury Detection Using Microwave Imaging

Sahar Borzooei, Pierre-Henri Tournier, Victorita Dolean, Christian Pichot, *Life Fellow, IEEE*, Nadine Joachimowicz, Helene Roussel, and Claire Migliaccio, *Member, IEEE*

***Abstract*—Rotator cuff tear (RCT) is one of the most common shoulder injuries, which can be irreparable if it develops to a severe condition. A portable imaging system for the on-site detection of RCT is necessary to identify its extent for early diagnosis. We introduce a microwave tomography system, using state-of-the-art numerical modeling and parallel computing for detection of RCT. The results show that the proposed method is capable of accurately detecting and localizing this injury in different size. In the next step, an efficient design in terms of computing time and complexity is proposed to detect the variations in the injured model with respect to the healthy model. The method is based on finite element discretization and uses parallel preconditioners from the domain decomposition method to accelerate computations. It is implemented using the open source FreeFEM software.**

***Index Terms*—Microwave imaging, parallel computation, inverse problem, regularization, shoulder injury.**

I. Introduction

RCT accounts for 70% of shoulder pain and dysfunction in adults [1]. It can be caused by a variety of factors, including age-related degeneration, overuse and acute injury [2]. RCTs are found in around 20% of 60 a olds, 30% of 70 a olds, and 50% of 80 a olds [3]. Rotator cuff repair incidence in the United States is reported over 15 per 103 people in 2006 [4]. Rotator cuff is a group of muscles and their tendons that work together to stabilize the shoulder, elevate and rotate the arm [5]. Most of the RCTs occur in the supraspinatus tendon [6]. A front view of the shoulder joint and RCT is shown in Fig. 1.[1] There are two types of RCTs: partial and complete. A partial tear is when the tendon of the rotator cuff is damaged but not completely severed. A complete tear is when the soft tissue is detached from the bone. Complete tears can be categorized as small, medium or large and massive [7]. The severity of RCT does not correlate with the pain experience and it can also be without symptoms, making it challenging to diagnose [8]. In addition, early detection of a partial RCT can help in preventing its development to full tear and may allow for nonsurgical treatment options [9]. After surgery, healing rate decreases with increased tear size as for small tears 66%, medium tears 68%, large tears 47%, and massive tears 27% [10]. This shows the importance of early diagnosis of this incidence. The standard imaging modalities being used to assess the presence and size of RCTs are magnetic resonance imaging (MRI), magnetic resonance angiography (MRA) and ultrasound (US) [11]. However, these methods are not always accurate in depicting the size and number of involved tendons [12], [13]. MRI as the first-choice imaging modality for the RCTs detection is costly, bulky and is not suitable for on-site early detection. There is frequent intra-operative reports claiming to find tears much larger than determined on MRI, or even the lack of a tear [14]. MRA is an invasive procedure that requires the injection of a contrast agent [15]. US is operator-dependent and limited by the patients body habitus [16]. An alternative low-cost, portable and non-invasive method is in demand for on-site preliminary diagnosis of RCTs, specifically for competitive athletes such as tennis players or swimmers [17], [18]. Portable electromagnetic imaging (EMI) systems have shown promising results as an early stage diagnosis method, which can lessen the burden on MRI usage [19], [20], [21]. The mobile approach can enable imaging of patients with mobility challenges, when they live in long distances from the imaging centers or are unable to travel to these centers [22]. Fully circular tomographic-based EMI systems are

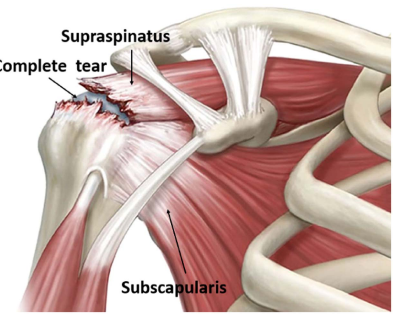

Fig. 1. Shoulder anatomy.

Manuscript received 30 October 2023; revised 28 February 2024 and 13 April 2024; accepted 23 May 2024. Date of publication 19 June 2024; date of current version 20 August 2024. This project has received funding from the European Union's Horizon 2020 research and innovation programme under Grant N 847581. It has been co-funded by the Region Provence-Alpes-Côte d'Azur and IDEX UCA^{JEDI} and supported by National Research Agency (ANR) under Reference ANR-15-IDEX-01. *(Corresponding author: Sahar Borzooei.)*

Sahar Borzooei, Victorita Dolean, Christian Pichot, and Claire Migliaccio are with the Université Côte d'Azur, 06103 Nice, France (e-mail: sahar.borzooei@etu.univ-cotedazur.fr).

Pierre-Henri Tournier is with CNRS, Université Paris Cité, Inria, Laboratoire Jacques-Louis Lions (LJLL), Sorbonne Université, F-75005 Paris, France.

Nadine Joachimowicz is with Sorbonne Université, CNRS, Laboratoire de Génie Electrique et Electronique de Paris, 75252 Paris, France, and also with the Université Paris Cité, F-75006 Paris, France.

Helene Roussel is with Sorbonne Université, CNRS, Laboratoire de Génie Electrique et Electronique de Paris, 75252 Paris, France.

Digital Object Identifier 10.1109/JERM.2024.3411799

[1][Online]. Available: https://www.cliniquedelepaule.com/rupture-coiffe-rotateurs/

designed for different applications, such as brain [23], [24], breast [25] and knee imaging [26]. Circular data acquisition effectively helps in increasing the cross-range resolution of the reconstructed images [27]. To the best of our knowledge, there is no EMI system to detect shoulder injuries. Designing an EMI system for shoulder is challenging due to following reasons. First, the complex anatomy of the shoulder prevents designing a fully circular phased array for spherical scan and full data acquisition. As a consequence, the antenna array has to be defined conformal to the shoulder geometry. Another challenge would be the electrically large size of the shoulder along with the heterogeneous nature of the tissues, characterized by high losses (also a characteristic of the matching medium), making it difficult to achieve a high resolution three-dimensional (3D) reconstruction. The shoulder being located in the near-field of the antenna array, an efficient 3D EM-modelling is required to consider coupling effects and near-field interactions between the imaging system and the shoulder. Besides, the variability in the shoulder anatomy among individuals prevents us to consider a particular shoulder structure as a priori knowledge. Finally, the accurate knowledge of the dielectric properties of the shoulder tissues, and more specifically the synovial fluid (SF), remains a challenge. At the early stage design, when assessing the potential of EMI on a new application, using numerical modeling to help designing the system presents several advantages: it allows to accurately model the human body complexity and electrical properties, and to simulate various anatomical scenarios in a flexible way, while reducing cost and time. In this paper, we propose a feasibility study based on numerical assessments to design a shoulder injury detection system and demonstrate its performance. We make use of an anthropomorphic numerical model of the shoulder and a built-in EM modeling based on the open source code FreeFEM. The paper is organized as follows: Section II discusses the dielectric properties of the shoulder tissues, while Section III describes the choices for a first shoulder imaging system with a dense number of antennas to achieve high resolution. The mathematical framework of the EM modeling is outlined in Section IV, and numerical solutions are presented in Section V. Section VI investigates the reduction of the number of antennas in the EMI system.

II. Dielectric Properties of the Shoulder Tissues

Once the RTCs occurs, SF accumulates at the location of the tear [28], [29] that leads to a change in the dielectric properties in the shoulder joint [30]. It is reported that the volume of SF on aspiration prior to arthroscopic rotator cuff repair correlates with tear size. The mean aspirate volume of partial tears is 0.76 ± 0.43 mL, small tears 1.46 ± 1.88 mL, medium tears 3.04 ± 2.21 mL, and large tears 6.60 ± 3.23 mL [29]. When there is a difference in the dielectric properties between different shoulder tissues and the SF, microwave imaging can detect this contrast. The larger the difference, the easier the detection. Thus, it is essential to measure the dielectric properties of the SF in relation to the other tissues. In a recent work with the purpose of detecting knee injury [26], high values of SF are considered compared to the rest of the tissues; however, to the best of our knowledge, no measurement of dielectric properties of SF is published in this or any other literature. It is reported that low frequencies ranging between $0.5-3$ GHz are suitable to achieve deeper tissue penetration as well as acceptable imaging quality [31]. In this section, the dielectric properties of the SF and the liquid mixtures mimicking the materials of muscle, bone cortical and tendons are measured in the frequency range of $1-4$ GHz. Four patients with knee or shoulder pain were sampled to obtain the real human SF. We computed the average value of the measured dielectric properties of the four SF samples, which had different temperature and pathology. The mixtures of the other tissues were made based on the SUPELEC RECIPES[2] [32]. An optimization code based on Kraszweski's binary law gives the concentration of TritonX-100 and salt required to produce mixtures, whose dielectric properties are close to those given by a Cole-Cole model, for each biological tissue of the shoulder region [33]. Measurements were performed using a homemade coaxial probe connected to a ZVH8 Vector Network Analyzer [34]. Fig. 2 gathers our measurements in dotted lines and the values from the references in solid lines for comparison [35], [36]. Our approach is in a good agreement with the references.

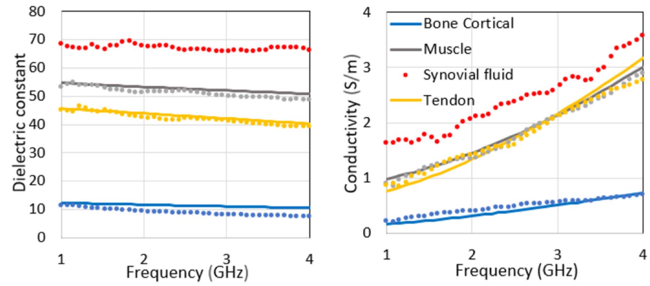

Fig. 2. Dielectric properties of the tissues.

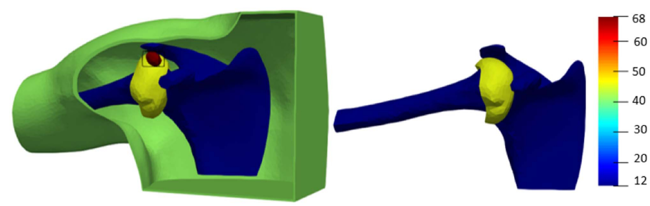

Fig. 3. Shoulder phantoms and real permittivity values.

The relative contrast between SF and other tissues over the frequency range of interest is around 30%, except for the muscle for which there is a 20% difference in the real part, making the tear detection feasible but challenging. The anthropomorphic shoulder model is shown in Fig. 3. The complex permittivity values of the shoulder tissues at 1 GHz are given in Table I and are used in the simulations. In this Table, the SF value corresponds to our measurements and the values of other tissues are the reference values, also available on the websites.[3, 4] The complex permittivity of the matching medium is chosen equal to that of the muscle.

[2][Online]. Available: http://applis.iut.univ-paris-diderot.fr/CNRS/
[3][Online]. Available: http://niremf.ifac.cnr.it/tissprop/
[4][Online]. Available: https://itis.swiss/virtual-population/tissue-properties/

TABLE I
COMPLEX DIELECTRIC PROPERTIES AT 1 GHZ

Region	Complex Permittivity	Color in Fig. 3
Bone cortical	$12.4 - 2.79j$	Blue
Tendon	$45.6 - 13.66j$	Yellow
Muscle	$54.8 - 17.43j$	Transparent
Skin	$40.9 - 16.17j$	Green
SF	$68.0 - 29.0j$	Red

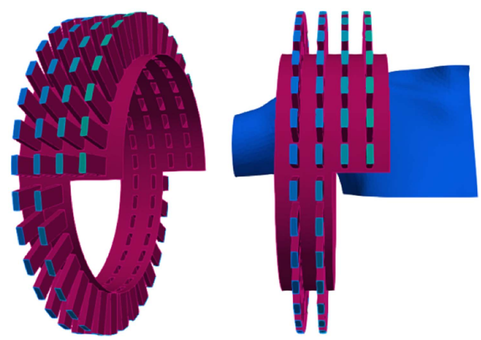

Fig. 4. EMI system for the shoulder.

III. ELECTROMAGNETIC IMAGING SYSTEM

We first design an EMI system with a dense array of antennas that illuminates the shoulder from different angles. This multi-view approach helps in reconstructing a comprehensive and accurate representation of the internal structures [37]. Results will be used as reference for the optimized system described in Section VI. The EMI system consists of 96 ceramic ($\varepsilon_r = 59$) loaded open-ended waveguides arranged on 2 metallic fully-circular and 2 metallic half-circular layers. The two sides of the imaging chamber are open. This wearable imaging system with open sides is adapted to the real shoulder structure and designed to surround it partially, as shown in Fig. 4. The width and height of the rectangular waveguides are 2.1 cm and 0.75 cm, respectively. Their frequency bandwidth is $0.93 - 1.85$ GHz. Here, the operating frequency of 1 GHz is chosen as a good compromise regarding penetration depth and low specific absorption rate (SAR) [38]. Considering the matching medium as the reference permittivity, the wavelength in this medium is $\lambda = 4.05$ cm. The diameter of the chamber is 7.407λ, the larger length is 3.11λ and the distance between antenna layers is 0.493λ. The larger size of the modeled large and partial tears is 0.72λ and 0.41λ, respectively. Note that we can expect a better resolution than 0.25λ, because EMI system is operating in the near field [39]. The space between antennas and the shoulder is filled with a matching medium to overcome air-skin reflections [40].

IV. MATHEMATICAL FRAMEWORK

A. Finite Element Mesh Generation

Finite element 3D mesh generation of the complete system is a challenging step due to both the complex geometry of the real body from and the imaging system components. For Finite element 3D mesh generation, we have used realistic surface Computer-Aided Design (CAD) models for shoulder profile and bones including humerus and scapula from a library of 3D models related to the anatomy.[5] A simple model of rotator cuff tendons was then built surrounding the shoulder joint. The skin is considered with a thickness of 2 mm surrounding the muscle geometry. The injury is modeled as an ellipsoid in the approximate location of the tear in the supraspinatus tendon, with two different size configurations. The regions corresponding to the different tissues are visible in Fig. 3. The remaining area (excluding bone, injury, tendon, skin) corresponds to the muscle. We built the 3D mesh of the complete system by giving special attention to the interfaces between domains to ensure that the mesh is well-aligned, conformal and continuous [41]. In this work, we use the open-source finite element software FreeFEM [42]. FreeFEM is interfaced with the MMG remeshing library which makes it possible to generate adapted tetrahedral meshes [43].

B. Forward Modeling

The 3D domain (Ω) includes the imaging system and the shoulder as a heterogeneous dissipative non-magnetic medium of complex permittivity $\varepsilon_r = (\varepsilon_r' - \frac{\sigma j}{\omega \varepsilon_0})$, with σ the conductivity, ε_r' relative permittivity of each tissue, ε_0 the permittivity of free space, and ω the angular frequency. In the frequency domain, the electric field $\mathbf{e}(\mathbf{x}, \mathbf{t}) = \Re(\mathbf{E}(\mathbf{x})e^{\mathrm{i}\omega \mathbf{t}})$ has harmonic dependence on time of angular frequency ω, where $\mathbf{E}(\mathbf{x})$ is its complex amplitude depending on the space variable $\mathbf{x}$. The boundary value problem is defined in (1).

$$\begin{cases} \nabla \times (\nabla \times \mathbf{E}) - k^2\mathbf{E} = 0, & \text{in } \Omega, \\ \mathbf{E} \times \mathbf{n} = 0, & \text{on } \Gamma_m \\ \nabla \times \mathbf{E} \times \mathbf{n} + \mathrm{i}\beta \mathbf{n} \times (\mathbf{E} \times \mathbf{n}) = g & \text{on } \Gamma_t \\ \nabla \times \mathbf{E} \times \mathbf{n} + \mathrm{i}\beta \mathbf{n} \times (\mathbf{E} \times \mathbf{n}) = 0 & \text{on } \Gamma_r \\ \nabla \times \mathbf{E} \times \mathbf{n} + \mathrm{i}k \mathbf{n} \times (\mathbf{E} \times \mathbf{n}) = 0 & \text{on } \Gamma_o, \end{cases} \tag{1}$$

where $\mathbf{E}(\mathbf{x})$ is the solution of equation (1) for each transmitting antenna and $k = \omega\sqrt{\varepsilon_r \varepsilon_0 \mu_0}$ is the complex wavenumber of the inhomogeneous medium, with μ_0 the permeability of free space. β is the propagation constant along the waveguide. The excitation term is defined as $g = 2\mathrm{i}\beta \mathbf{E}^{TE_{10}}$, imposing an incident wave corresponding to the excitation of the dominant transverse electric mode (TE_{10}) of the transmitting waveguide. Γ_t is the port of the transmitting waveguide, Γ_r corresponds to ports of receiving waveguides, Γ_m represents the metallic surfaces of the waveguides and the walls between them, and Γ_o represent the three open sides (right, left and bottom) of the chamber and the boundaries of shoulder profile. Through the solutions of (1) for each transmitting antenna, we compute the scattering matrix, a set of complex-valued reflection and transmission coefficients, given in equation (2):

$$S_{ij} = \frac{\int_{\Gamma_r} \mathbf{E} \cdot \mathbf{E}^{TE_{10}}}{\int_{\Gamma_r} |\mathbf{E}^{TE_{10}}|^2}. \tag{2}$$

The computed S_{ij} matrix of size 96×96 is used to produce synthetic data by adding a multiplicative white Gaussian noise.

[5] [Online]. Available: https://www.plasticboy.co.UK/store/index.html

The Gaussian noise is applied independently to the real and imaginary parts of each S_{ij} coefficient as independent random variables. To start, we have corrupted the data S_{ij} with 23 dB noise. The finite element discretization of our problem leads to a large ill-conditioned linear system $A\mathbf{u} = \mathbf{b}$ for each transmitting antenna. Domain decomposition methods (DDMs) are efficient tools to solve such large systems in parallel, both in terms of convergence and computing time [44], [45]. A Krylov iterative solver (GMRES) along with an Optimized Restricted Additive Schwarz (ORAS) preconditioner is chosen to solve our problem. The domain decomposition preconditioner is implemented in the HPDDM library [46], an open source high-performance unified framework for domain decomposition methods which is interfaced with the FreeFEM software.

C. Inverse Problem

Let $\kappa = k^2$ be the unknown complex parameter of the inverse problem in each point of Ω. In this step an optimization problem, including a fit-to-data term and a regularizing term, is defined with the following cost function:

$$J(\kappa) = \frac{1}{2}\sum_{j=1}^{N}\sum_{i=1}^{N}\frac{|S_{ij}(\kappa) - S_{ij}^{syn}|^2}{|S_{ij}^{empty}|^2} + \alpha R(\kappa). \quad (3)$$

where S_{ij}^{syn} are the scattering coefficients obtained from the forward problem and are referred to as synthetic data in the rest of the paper. S_{ij}^{κ} are the scattering coefficients computed for the unknown κ at the current iteration. S_{ij}^{empty} are the coefficients computed from the simulation when the domain is filled only with the homogeneous matching medium, used for normalization. N is the number of antennas of the system. We use the limited memory Broyden-Fletcher-Goldfarb-Shanno (L-BFGS) algorithm for optimization and the Tikhonov regularization method for reducing the noise effect, defined as $R(\kappa) = \frac{1}{2}\int_{\Omega}|\nabla\kappa|^2$. The regularization parameter α is chosen empirically equal to 10^{-6} to reach a good compromise between denoising as well as achieving suitable image quality with respect to certain properties such as smoothness or sparsity [47]. We refer to [48] for a detailed description of the inverse modeling that we have followed in this work. Note that we avoid inverse crime by adding noise to the synthetic data (explained in Section IV-B) and not using a priori knowledge of the body structure. Eliminating a priori knowledge is done by using a mesh that includes the geometry and structure of the body for generating synthetic data (Fig. 5, left) but defining a different homogeneous mesh that is limited to the imaging chamber (Fig. 5, right) for the inverse problem. Using Nedelec edge finite elements (FE) of first degree for the FE discretization results in 510531 unknowns for the forward problem and 357535 unknowns for the inverse problem. The spatial resolution for both generated meshes is the number of points per wavelength n_λ, here $n_\lambda = \frac{\lambda}{6}$, where λ corresponds to the wave propagation in the matching medium/muscle tissue.

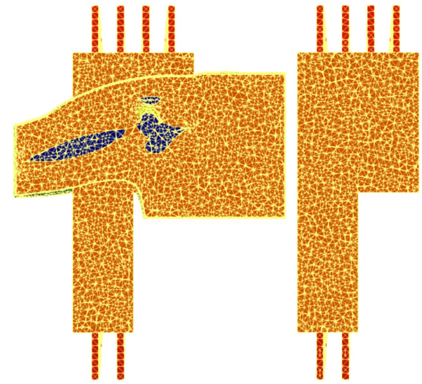

Fig. 5. Left: Synthetic data. Right: Inverse problem.

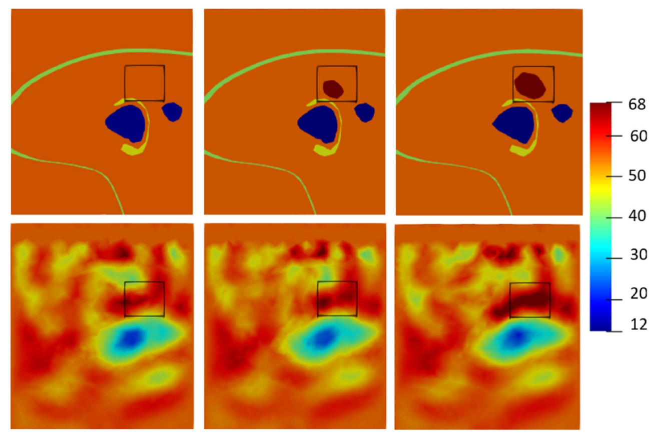

Fig. 6. Cross-section of the real part of the permittivity. Top: exact permittivity, bottom: reconstructed permittivity. From left to right: Healthy, partial tear and large tear.

V. Numerical Results

Results are obtained on the Université Côte d'Azur's High-Performance Computing (HPC) center. In this HPC center, cluster is composed of 48 CPU computing nodes, including 32 nodes with Dual Intel Xeon Gold processor, providing 40 cores per node and 192 GB of memory and 16 nodes with 2 AMD Epyc processors, providing 32 cores per node and 256 GB of memory. The simulations presented in this paper were carried out using 480 cores. Each reconstruction starts from an initial guess of homogeneous matching medium. The reconstruction results shown here are obtained after 60 iterations; the residual is decreased by a factor of 10^{-2}. Subsequent iterations do not provide any further noteworthy decrease. Figs. 6 and 7 show a cross section of the exact (top) and reconstructed (bottom) results for healthy, partially injured (1 mL SF) and fully injured (5 mL SF) shoulder on the regions of interest. Note that in the healthy shoulder case, the ellipsoid is filled in with muscle as shown in Figs. 6 and 7 for comparison purpose. The tear is visible in reconstructed real and imaginary parts. For a better view, we also plot the difference between reconstructed permittivity of healthy case and those for the partially and largely injured cases, known as differential images [49]. They are shown for the magnitude of the ε_r in Fig. 8, proving that the inverse algorithm succeeds in detecting the injury, with respect to size and location, even

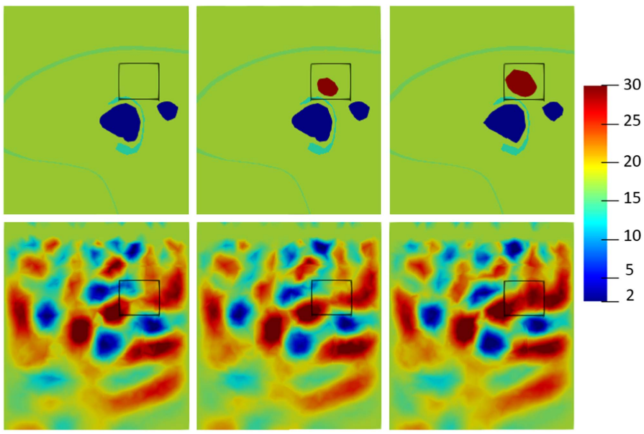

Fig. 7. Cross-section of the imaginary part of the permittivity. Top: exact permittivity, bottom: reconstructed permittivity. From left to right: Healthy, partial tear and large tear.

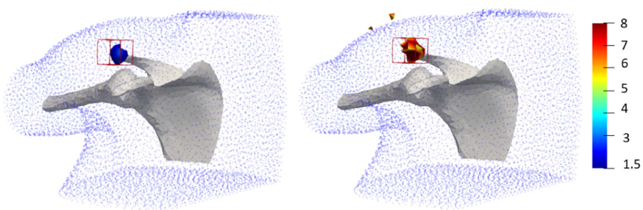

Fig. 8. The differential image ($|\varepsilon_r|$) for partial and large tear.

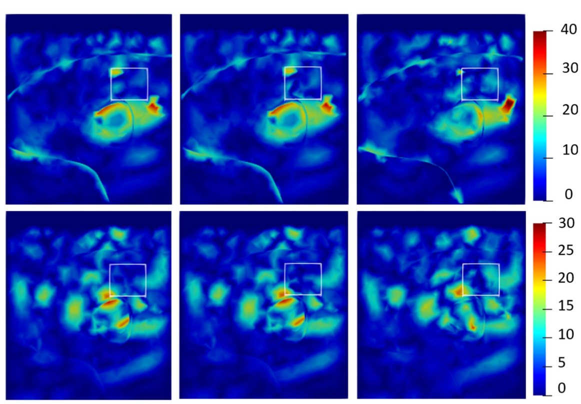

Fig. 9. The absolute error. Top: real part, bottom: Imaginary part. From left to right: Healthy shoulder, partial and large tear.

for the partial tear.

$$err_{absolute} = |\varepsilon_r^{reconstructed} - \varepsilon_r^{exact}| \tag{4}$$

The reconstruction is further assessed by computing the absolute error on the real and imaginary parts according to (4) applied on each pixel of the reconstructed domain. Results are shown in Fig. 9. Error distribution is not uniform across tissues. Highest values are on the edges of the bone area, due to the higher contrast between the complex permittivity of bone and muscle. However, inside the bone in the areas that are not in the vicinity of the edges, the error decreases as expected, due to better performance of the inversion algorithm in a homogeneous region compared to the interfaces. The minimum values of the absolute error in the injury area are 0.78 and 0.435, respectively for the real and imaginary parts of the partial tear. These values for the large tear

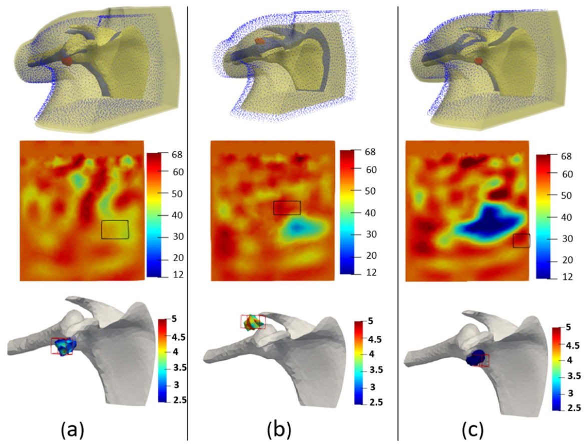

Fig. 10. From top to bottom: phantom variation, solution on the real part of the injured model and the differential image ($|\varepsilon_r|$). Scale ratio for (a) is 1.11, for (b) is 0.85 and for (c) is 1.05.

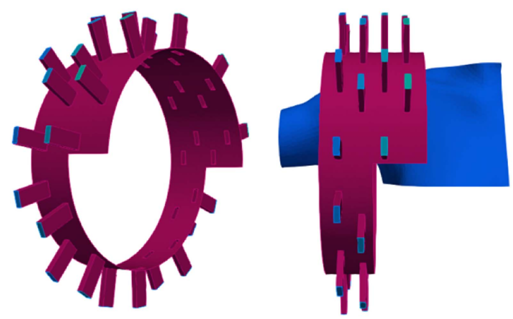

Fig. 11. Optimal shoulder EMI system.

are 0.0088 and 0.065, respectively. To further assess the image reconstruction, 3 different variations of the phantoms of different size and different realistic location of injury are studied in each column. In Fig. 10, the new phantoms are shown in yellow which are changed with different scale ratios in three directions. The reference phantom of Fig. 8 is shown in blue for comparison. The volume of injuries are 4.5 mL for (a) and 2.5 mL for (b) and (c). We can see that the tears are detectable for all cases, however for (c) it is more difficult compared to the others, due to its placement under the bone and lack of antennas in that part.

VI. An Improved Design of EMI System

In this section, an efficient design of the imaging system in terms of reduced number of antennas is proposed. With less transmitting and receiving waveguides, faster computing time as well as cost-effective design can be achieved. The system is optimized according to the following guidelines:

- The number of antennas is a power of two to ease practically feeding signals into a switching matrix.
- We introduce a spatial shift between antennas of adjacents rings as shown in Fig. 11, in order to preserve the spatial diversity.

Different design configurations are assessed based on the value of the L^2 norm relative error, referred to as err according to (5), as well as the mean value of the subtraction between the reconstructed injured model and reconstructed healthy model in

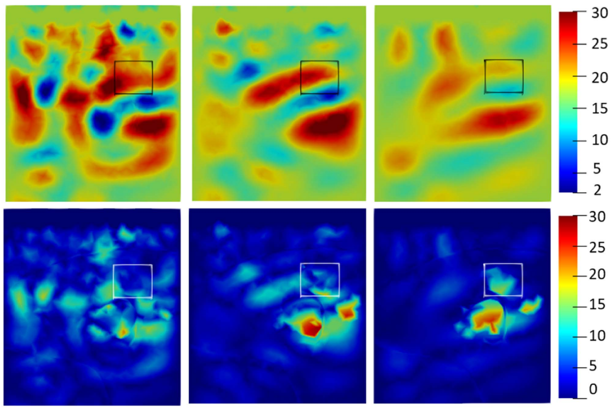

Fig. 12. Top: Solution on the imaginary part, bottom: absolute error on the imaginary part. From left to right: $N = 64$, $N = 32$, $N = 16$.

TABLE II
err IN THE INJURY AREA AND TOTAL DOMAIN FOR THE PARTIAL TEAR CASE, AND COMPUTING TIME

N	Total		Injury		time
	real	imaginary	real	imaginary	(min:s)
96	8.8%	21.4%	14%	24.4%	20 : 09
64	9.0%	21.2%	10.4%	19.2%	16 : 24
32	9.4%	20.6%	16.8%	33.3%	12 : 02
16	10.8%	17.2%	19.3%	45.9%	11 : 27

TABLE III
ctr IN THE INJURY AREA FOR PARTIAL AND LARGE TEARS WITH DIFFERENT NOISE LEVELS

	N	Noise of 23 dB		Noise of 15 dB		Noise of 10 dB	
		real	imaginary	real	imaginary	real	imaginary
Partial	96	1.803	1.910	1.934	1.767	1.973	1.696
	64	1.605	1.673	1.664	1.654	2.233	1.503
	32	0.890	0.690	0.843	0.669	0.599	0.681
	16	0.133	0.1918	−0.136	0.0193	0.3617	0.256
Large	96	5.254	5.101	5.182	5.230	5.412	5.033
	64	5.053	4.312	5.145	4.310	5.396	4.244
	32	2.322	2.241	2.467	2.191	2.524	2.204
	16	0.750	0.711	0.692	0.681	0.787	0.780

the injured area, defined in (6). Three different configurations are considered, with 16, 32, and 64 antennas; the reference configuration corresponds to the complete system with 96 antennas. In Fig. 12, the solution and the absolute error for imaginary part of largely injured model are shown for reduced N. It is visible that the presence of injury in solution fades with decreasing number of antennas, while the error in the injury area increases. The values of err for each configuration are computed in the whole domain as well as in the injury area for the partially injured model and are gathered in Table II. Looking at the err values on both real and imaginary parts, there is no significant increase when reducing the number of antennas by 64 ($N = 32$). However, further removing 16 antennas and going from $N = 32$ to $N = 16$ antennas leads to a higher increase in err. In order to make the decision about N, we look at the contrast (ctr) between the healthy and the injured shoulder model. It has to be positive at the tear location, since the SF has an higher ε_r compared to the rest of the tissues. The contrast values are shown in Table III for both partial and large tear and with different levels of noise. In the partial tear case, the value of ctr remains positive notable for $N = 32$ for all noise levels, and we expect to be able to detect the injury. In contrast, ctr is either negligible or negative for $N = 16$, resulting in poor differential images. The $N = 32$ configuration is chosen as our best compromise design which still allows detection of the most difficult partial tear as seen by the positive ctr for all investigated noise levels. This was further confirmed by extracting and comparing the differential images for each configuration, but due to space limitation the images are not shown in the paper. The optimal $N = 32$ antennas configuration is depicted in Fig. 11 and has 11 and 10 antennas in both full layers and 6 and 5 antennas on both half layers, from left to right. Note that the computing time decreases to about half of the required time for the full $N = 96$ configuration.

$$err = \frac{||\varepsilon_r^{reconstructed} - \varepsilon_r^{exact}||_2}{||\varepsilon_r^{exact}||_2} \tag{5}$$

$$ctr = \varepsilon_r^{injured} - \varepsilon_r^{healthy} \tag{6}$$

VII. CONCLUSION

We have conducted the first numerical study on the feasibility to image the shoulder joint with an EMI system. The first part of the study consisted in the investigation of the dielectric properties of the shoulder tissues, in particular the synovial fluid which was measured for the first time. Secondly, we have shown that it is possible to reconstruct 3D images of the shoulder joint based on an anthropomorphic numerical model of the shoulder with an imaging system composed of 96 antennas. The reconstruction takes 20 minutes and 9 seconds on 480 computing cores and shows great promise for rapid diagnosis or medical monitoring. Finally, we take advantage of numerical modeling to optimize the number of antennas in the EMI system. We achieve a drastic reduction from 96 to 32 antennas. After having proved the relevance of microwave imaging for the detection of shoulder injury, the next step will be to move on the experimental phase.

ACKNOWLEDGMENT

The authors like to thank Dr Eric GIBERT, rheumatologist at the Pitié-Salpêtrière Hospital in Paris, for providing the SF samples for dielectric characterization. The authors are grateful to the OPAL infrastructure from Université Côte d'Azur and the Université Côte d'Azur's Center for High-Performance Computing for providing resources and support.

REFERENCES

[1] B. J. Mera, "Current perspectives on rotator cuff disease," *Osteology*, vol. 2, no. 2, pp. 62–69, 2022.

[2] R. W. Nyffeler, N. Schenk, and P. Bissig, "Can a simple fall cause a rotator cuff tear? Literature review and biomechanical considerations," *Int. Orthopaedics*, vol. 45, pp. 1573–1582, 2021.

[3] H. Minagawa et al., "Prevalence of symptomatic and asymptomatic rotator cuff tears in the general population: From mass-screening in one village," *J. Orthopaedics*, vol. 10, no. 1, pp. 8–12, 2013.

[4] A. C. Colvin, N. Egorova, A. K. Harrison, A. Moskowitz, and E. L. Flatow, "National trends in rotator cuff repair," *J. Bone Joint Surgery. Amer. Volume*, vol. 94, no. 3, 2012, Art. no. 227.

[5] J. R. Dugas, D. A. Campbell, R. F. Warren, B. H. Robie, and P. J. Millett, "Anatomy and dimensions of rotator cuff insertions," *J. Shoulder Elbow Surg.*, vol. 11, no. 5, pp. 498–503, 2002.

[6] R. Omid and B. Lee, "Tendon transfers for irreparable rotator cuff tears," *J. Amer. Acad. Orthopaedic Surgeons*, vol. 21, no. 8, pp. 492–501, 2013.

[7] U. G. Longo, A. Berton, W. S. Khan, N. Maffulli, and V. Denaro, "Histopathology of rotator cuff tears," *Sports Med. Arthroscopy Rev.*, vol. 19, no. 3, pp. 227–236, 2011.

[8] A. Yamamoto et al., "The impact of faulty posture on rotator cuff tears with and without symptoms," *J. Shoulder Elbow Surg.*, vol. 24, no. 3, pp. 446–452, 2015.

[9] A. Abdelwahab, N. Ahuja, K. P. Iyengar, V. K. Jain, N. Bakti, and B. Singh, "Traumatic rotator cuff tears-current concepts in diagnosis and management," *J. Clin. Orthopaedics Trauma*, vol. 18, pp. 51–55, 2021.

[10] M. S. Rashid et al., "Increasing age and tear size reduce rotator cuff repair healing rate at 1 year: Data from a large randomized controlled trial," *Acta Orthopaedica*, vol. 88, no. 6, pp. 606–611, 2017.

[11] J. P. Iannotti et al., "Accuracy of office-based ultrasonography of the shoulder for the diagnosis of rotator cuff tears," *J. Bone Joint Surg.*, vol. 87, no. 6, pp. 1305–1311, 2005.

[12] S. A. Teefey, D. A. Rubin, W. D. Middleton, C. F. Hildebolt, R. A. Leibold, and K. Yamaguchi, "Detection and quantification of rotator cuff tears: Comparison of ultrasonographic, magnetic resonance imaging, and arthroscopic findings in seventy-one consecutive cases," *J. Bone Joint Surg.*, vol. 86, no. 4, pp. 708–716, 2004.

[13] Y. Shibayama et al., "Diagnostic accuracy of magnetic resonance imaging for partial tears of the long head of the biceps tendon in patients with rotator cuff tears," *JSES Int.*, vol. 6, no. 4, pp. 638–642, 2022.

[14] X. Li, Q. Hou, X. Zhan, L. Chang, X. Ma, and H. Yuan, "The accuracy of MRI in diagnosing and classifying acute traumatic multiple ligament knee injuries," *BMC Musculoskelet. Disord.*, vol. 23, pp. 1–7, 2022.

[15] A. Yip et al., "Magnetic resonance imaging compared to ultrasonography in giant cell arteritis: A cross-sectional study," *Arthritis Res. Ther.*, vol. 22, no. 1, pp. 1–8, 2020.

[16] M. Adrian, "MRI: Understanding its limitations," *Brit. Columbia Med. J.*, vol. 47, pp. 359–361, 2005.

[17] V. Upadhyaya and H. N. Choudur, "Update on sports imaging," *J. Clin. Orthopaedics Trauma*, vol. 21, 2021, Art. no. 101555.

[18] J. Stahnke, M. Schenk, and K. Sharpe, "Magnetic resonance imaging of symptomatic swimmer's shoulder," *Int J. Radiol. Imag. Technol*, vol. 6, 2020, Art. no. 070.

[19] I. Amdaouch et al., "A novel approach of a low-cost UWB microwave imaging system with high resolution based on SAR and a new fast reconstruction algorithm for early-stage breast cancer detection," *J. Imag.*, vol. 8, no. 10, 2022, Art. no. 264.

[20] M. Islam, M. Mahmud, M. T. Islam, S. Kibria, and M. Samsuzzaman, "A low cost and portable microwave imaging system for breast tumor detection using UWB directional antenna array," *Sci. Rep.*, vol. 9, no. 1, 2019, Art. no. 15491.

[21] M. S. Islam, M. T. Islam, and A. F. Almutairi, "A portable non-invasive microwave based head imaging system using compact metamaterial loaded 3D unidirectional antenna for stroke detection," *Sci. Rep.*, vol. 12, no. 1, 2022, Art. no. 8895.

[22] S. C. Deoni et al., "Development of a mobile low-field MRI scanner," *Sci. Rep.*, vol. 12, no. 1, 2022, Art. no. 5690.

[23] P.-H. Tournier et al., "Numerical modeling and high-speed parallel computing: New perspectives on tomographic microwave imaging for brain stroke detection and monitoring," *IEEE Antennas Propag. Mag.*, vol. 59, no. 5, pp. 98–110, Oct. 2017.

[24] M. Hopfer, R. Planas, A. Hamidipour, T. Henriksson, and S. Semenov, "Electromagnetic tomography for detection, differentiation, and monitoring of brain stroke: A virtual data and human head phantom study," *IEEE Antennas Propag. Mag.*, vol. 59, no. 5, pp. 86–97, Oct. 2017.

[25] C. Zellweger et al., "Breast computed tomography: Diagnostic performance of the maximum intensity projection reformations as a stand-alone method for the detection and characterization of breast findings," *Invest. Radiol.*, vol. 57, no. 4, pp. 205–211, 2022.

[26] K. Sultan, "Design and implementation of electromagnetic knee imaging systems," Ph.D. dissertation, Sch. Inf. Technol. Electr. Eng., Univ. Queensland 2022, doi: 10.14264/d377054.

[27] L. Wang, "Microwave imaging and sensing techniques for breast cancer detection," *Micromachines*, vol. 14, no. 7, 2023, Art. no. 1462.

[28] A. Papatheodorou, P. Ellinas, F. Takis, A. Tsanis, I. Maris, and N. Batakis, "US of the shoulder: Rotator cuff and non–rotator cuff disorders," *Radiographics*, vol. 26, no. 1, 2006, Art. no. e23.

[29] M. Stone, G. Jamgochian, O. Thakar, M. S. Patel, and J. A. Abboud, "Synovial fluid volume at the time of arthroscopic rotator cuff repair correlates with tear size," *Cureus*, vol. 12, no. 7, 2020, Art. no. e9224.

[30] J. Kiel and E. Olwell, "It might be a tumor: A unique presentation of a chronic rotator cuff tear," *Afr. J. Emerg. Med.*, vol. 10, no. 4, pp. 288–290, 2020.

[31] N. K. Nikolova, "Microwave imaging for breast cancer," *IEEE Microw. Mag.*, vol. 12, no. 7, pp. 78–94, Dec. 2011.

[32] N. Joachimowicz, B. Duchêne, C. Conessa, and O. Meyer, "Anthropomorphic breast and head phantoms for microwave imaging," *Diagnostics*, vol. 8, no. 4, 2018, Art. no. 85. [Online]. Available: http://applis.iut.univ-paris-diderot.fr/CNRS/

[33] S. Gabriel, R. Lau, and C. Gabriel, "The dielectric properties of biological tissues: III. parametric models for the dielectric spectrum of tissues," *Phys. Med. Biol.*, vol. 41, no. 11, 1996, Art. no. 2271.

[34] S. Abedi, H. Roussel, and N. Joachimowicz, "Standardized phantoms," in *Electromagnetic Imaging for a Novel Generation of Medical Devices: Fundamental Issues, Methodological Challenges and Practical Implementation*. Berlin, Germany: Springer, 2023, pp. 1–32.

[35] P. Hasgall et al., "IT'IS database for thermal and electromagnetic parameters of biological tissues," Version 4.1, Feb. 22, 2022. [Online]. Available: https://itis.swiss/virtual-population/tissue-properties/

[36] R. D. Andreuccetti and C. Petrucci, "An Internet resource for the calculation of the dielectric properties of body tissues in the frequency range 10 Hz 100 GHz IFAC-CNR, Florence (Italy), 1997. Based on data published by C.Gabriel et al. in 1996," 2022. [Online]. Available: http://niremf.ifac.cnr.it/tissprop/

[37] C. Liu, B. Zhang, C. Xue, W. Zhang, G. Zhang, and Y. Cheng, "Multi-perspective ultrasound imaging technology of the breast with cylindrical motion of linear arrays," *Appl. Sci.*, vol. 9, no. 3, 2019, Art. no. 419.

[38] K. S. Sultan, A. Mahmoud, and A. M. Abbosh, "Textile electromagnetic brace for knee imaging," *IEEE Trans. Biomed. Circuits Syst.*, vol. 15, no. 3, pp. 522–536, Jun. 2021.

[39] T. J. Cui, W. C. Chew, X. X. Yin, and W. Hong, "Study of resolution and super resolution in electromagnetic imaging for half-space problems," *IEEE Trans. Antennas Propag.*, vol. 52, no. 6, pp. 1398–1411, Jun. 2004.

[40] H.-S. Lui, A. Fhager, and M. Persson, "Matching medium for biomedical microwave imaging," in *Proc. IEEE Int. Symp. Antennas Propag.*, 2015, pp. 1–3.

[41] R. M. J. Kramer and D. R. Noble, "Guaranteed quality conformal mesh decomposition," Sandia Nat. Lab., Albuquerque, NM, USA, Tech. Rep. SAND2015-11119J, 2015.

[42] F. Hecht, "New development in freefem," *J. Numer. Math.*, vol. 20, no. 3/4, pp. 251–266, 2012.

[43] C. Dobrzynski, "MMG3D: User guide," *HAL*, INRIA, Tech. Rep. RT-0422, 2012.

[44] N. Bootland, S. Borzooei, V. Dolean, and P.-H. Tournier, "Numerical assessment of PML transmission conditions in a domain decomposition method for the helmholtz equation," in *Proc. Int. Conf. Domain Decomposition Methods*, 2022, pp. 445–453.

[45] S. Borzooei, V. Dolean, P.-H. Tournier, and C. Migliaccio, "Solution of time-harmonic maxwell's equations by a domain decomposition method based on PML transmission conditions," in *Proc. Int. Conf. Sci. Comput. Elect. Eng.*, 2022, pp. 45–52.

[46] P. Jolivet, F. Hecht, F. Nataf, and C. Prud'Homme, "Scalable domain decomposition preconditioners for heterogeneous elliptic problems," in *Proc. Int. Conf. High Perform. Comput. Netw. Storage Anal.*, 2013, pp. 1–11.

[47] Y. Zheng, M. Li, J. Zhang, and J. Wang, "Selection of regularization parameter in GMM based image denoising method," *Multimedia Tools Appl.*, vol. 77, pp. 30121–30134, 2018.

[48] P.-H. Tournier et al., "Microwave tomographic imaging of cerebrovascular accidents by using high-performance computing," *Parallel Comput.*, vol. 85, pp. 88–97, 2019.

[49] R. Scapaticci et al., "Differential microwave imaging for brain stroke followup," *Int. J. Antennas Propag.*, vol. 2014, pp. 1–11, 2014.

Sahar Borzooei received the M.S. degree in electrical engineering (telecommunication, field and wave), in 2017. She is currently working toward the Ph.D. degree with Jean Alexandre Dieudonné Laboratory, CNRS, Université Côte d'Azur, Nice, France. Her research interests include microwave imaging systems for medical applications, domain decomposition methods, and machine learning algorithms.

Pierre-Henri Tournier received the Ph.D. degree from the University Pierre and Marie Curie (UPMC-Paris 6), Paris, France, in 2015. He is currently a Research Engineer with the Jacques-Louis Lions Laboratory, Sorbonne University, Paris, French National Center for Scientific Research (CNRS), Paris. He works on devising and implementing robust and efficient parallel numerical algorithms. His research focuses on linear solvers for large scale problems using domain decomposition methods, in particular for wave propagation problems.

Victorita Dolean received the Ph.D. degree from the University of Nice, Nice, France, in 2001. She is currently a Full Professor with TU Eindhoven, Eindhoven, The Netherlands, and a Visiting Professor with the University of Strathclyde, Glasgow, U.K. She is also a Fellow of the Institute of Mathematics and its Applications. She was a Postdoc with CMAP of Ecole Polytechnique, Paris. She works on the design of fast algorithms for the simulation of complex systems of PDEs with a focus in the latest years on wave propagation problems. She has coauthored a reference work on Domain decomposition methods (published by SIAM in 2015). Together with her collaborators, she was the recipient of Bull-Joseph Fourier Prize, delivered by Atos-Bull, for her innovative work on real time simulation of strokes using HPC.

Christian Pichot (Life Fellow, IEEE) received the Ph.D. and the D.Sc. degrees from the University of Paris-Sud, Orsay, France, in 1977 and 1982, respectively. He is currently the Director of Research Emeritus CNRS (National Center for Scientific Research), Electronics, Antennas & Telecommunications Laboratory (LEAT), joint Université Côte d'Azur, Nice, France, and CNRS laboratory, Sophia Antipolis, France.

In 1978, he joined the Systems and Signals Laboratory, Supélec, Gif-sur-Yvette, France. From 1989 to 1990, he was a Visiting Researcher with the Lawrence Livermore National Laboratory, Livermore, CA, USA. From 1993 to 1995, he was with the Sophia Antipolis Computer Science, Signals and Systems Laboratory, University Nice-Sophia Antipolis-CNRS, Valbonne, France. In 1996, he joined the Electronics, Antennas & Telecommunications Laboratory (LEAT), where he was the Director from 2000 to 2011. From 2008 to 2013, he was the Co-Director of CREMANT, a joint Antenna Research Center, supported by the University of Nice-Sophia Antipolis, CNRS, and France Telecom Orange Labs, Sophia Antipolis. In 2018, he was a Guest Professor with Mälardalen University, Västerås, Sweden, in 2018, and a Visiting Professor, Ming Hsieh Department of Electrical and Computer Engineering, University of Southern California, Los Angeles, CA, USA, during Jan–Mar. 2020.

His current research interests include the scattering and propagation of electromagnetic waves, radiation of antennas, inverse scattering (microwave imaging and tomography, antenna synthesis, complex permittivity reconstruction, and object detection and recognition) for applications in radar, civil engineering, nondestructive evaluation, geophysics engineering, security and military applications. He is an IEEE Fellow for Contributions to Microwave Imaging and Antenna Design. He was the recipient of the European Microwave Prize in 1983. He has been the Organizer and General Chair of the IEEE International Conference on Antenna Measurements and Applications (IEEE CAMA) since 2014. He is actually a member of the IEEE AP-S New Technology Directions Committee (NTDC), now Technical Directions Committee (TDC) and IEEE AP-S SIGHT (Special Interest Group on Humanitarian Technology). He was the recipient of the French Academy of Science URSI-France Medal in 2020.

Nadine Joachimowicz received the Ph.D. degree from the Université Paris Cité, Paris, France, in 1990. She joined the Electromagnetics Department of the Laboratoire des Signaux et Systémes in 1987, and the Group of Electrical Engineering Paris - GeePs, in 2015. Since 1993, she has been a Lecturer-Researcher with the University Institute of Technology, IUT de Paris Pajol, Paris. Her research activities are concerned with 2D and 3D scattering, direct and inverse problems in inhomogeneous media. She is currently involved in the conception and development of biological phantoms for the development and evaluation of microwave imaging systems.

Helene Roussel received the Ph.D. degree from University Pierre and Marie Curie (UPMC-Paris 6), Paris, France, in 1993. She has been a Professor with Sorbonne Université, Paris, since 2009, and her research is done with the Laboratory GeePs, joint unit of CNRS, Sorbonne Université, CentraleSupelec and Paris Saclay University, Paris. Her research interests include numerical methods and fast algorithms for electromagnetic scattering and radiation in complex media focusing on applications for metamaterials and on the analysis of wave propagation and scattering in complex media for target detection, medical imaging, and radar remote sensing.

Claire Migliaccio (Member, IEEE) received the Engineer degree in 1993 and the Ph.D. degree from INP Grenoble, Grenoble, France, in 1996. After her degrees, she was appointed as an Assistant Professor with Université Côte d'Azur where she became Full Professor in 2007. Her research interests include microwave to millimeter-wave systems for radar and imaging applications, including antenna design, measurements, and imaging techniques. Her main achievements deal with mm-Wave radar for rescue helicopters or FOD detection and mm-Wave scanners for security, food safety, and archaeological applications. Since 2020, she has been committed to promoting diversity, equity, inclusion and a sense of belonging through the committee she created and which bears the same name within IEEE AP-S. She is also the Founder and Chair of the IEEE AP-S Mojgan Daneshmand Grant for Women.